Influence of intermolecular potentials on rarefied gas flows: fast spectral solutions of the Boltzmann equation

Physics of Fluids (2015) 27:082002

Influence of intermolecular potentials on rarefied gas flows: fast spectral solutions of the Boltzmann equation

Lei Wu,[1, a)] Haihu Liu,[2] Yonghao Zhang,[1] and Jason M. Reese[3]

[1)] *James Weir Fluids Laboratory, Department of Mechanical and Aerospace Engineering, University of Strathclyde, Glasgow G1 1XJ, UK*

[2)] *School of Energy and Power Engineering, Xi'an Jiaotong University, 28 West Xianning Road, Xi'an 710049, China*

[3)] *School of Engineering, University of Edinburgh, Edinburgh EH9 3JL, UK*

The Boltzmann equation with an arbitrary intermolecular potential is solved by the fast spectral method. As examples, noble gases described by the Lennard-Jones potential are considered. The accuracy of the method is assessed by comparing both transport coefficients with variational solutions and mass/heat flow rates in Poiseuille/thermal transpiration flows with results from the discrete velocity method. The fast spectral method is then applied to Fourier and Couette flows between two parallel plates, and the influence of the intermolecular potential on various flow properties is investigated. It is found that for gas flows with the same rarefaction parameter, differences in the heat flux in Fourier flow and the shear stress in Couette flow are small. However, differences in other quantities such as density, temperature, and velocity can be very large.

[a)] Electronic mail: lei.wu.100@strath.ac.uk

I. INTRODUCTION

When the ratio of the molecular mean free path to the characteristic flow length becomes significant, the Boltzmann equation (BE) is the best tool to investigate the rarefied gas dynamics[1]. The BE employs a one-particle velocity distribution function (VDF) to describe the state of a macroscopic volume of gas consisting of a large number of molecules, where the linear streaming operator models the molecular transport and the nonlinear Boltzmann collision operator (BCO) describes the binary molecular collisions.

The intermolecular potential is incorporated into the BCO through the differential cross-section (DCS). As the DCSs for realistic potentials such as Lennard-Jones (LJ) or the potentials from *ab initio* calculations are very complicated, the simple hard-sphere (HS) model with a constant value of DCS is widely adopted[2]. However, the viscosity and heat conductivity of the HS model are proportional to the square root of the gas temperature, which does not agree with experimental data for common gases. To overcome this drawback, variable HS[2], variable soft-sphere[3], generalized HS[4], and generalized soft-sphere[5] models have been proposed for the direct simulation Monte Carlo (DSMC) simulation of the BE. Also, the μ-DSMC method has been proposed in order to reproduce an arbitrary viscosity variation with temperature[6]. In our recent fast spectral approximation of the BCO, some special forms of the DCS were used to recover Sutherland's formula for viscosity, as well as the viscosity of the LJ potential[7,8].

Note that all these DCSs were proposed in order to match the viscosity, and sometimes the mass diffusion coefficient, with experimental data or theoretical values, but they ignore or simplify the detailed dependence of the DCS on the deflection angle and the relative collision energy that are characteristic of realistic potentials. For gas mixtures, the use of simplified DCSs becomes problematic, since it is difficult to recover the mass diffusion and thermal diffusion coefficients simultaneously for general intermolecular potentials. As the intermolecular potential can strongly influence certain phenomena in rarefied gases[9,10], a numerical method to solve the BE with realistic potentials is urgently needed.

Implementation of the LJ potential in DSMC has been reported previously[11], but was time-consuming as the deflection angle was calculated for every binary collision. Recently, the LJ potential and some *ab initio* potentials were successfully implemented into the DSMC method by pre-calculating the deflection and storing the results in a table[12–14]. Alternatively,

an LJ polynomial approximation model was proposed to represent the deflection angle as a polynomial expansion in non-dimensional collision parameters[15,16]. Realistic intermolecular potentials have also been used in some deterministic numerical methods for solutions of the BE[10,17,18]. However, the discrete velocity method developed for the linearized BE[10,17] has a very high computational cost, which means it can only be applied to simple geometries, while the accuracy of the projection-interpolation method[18] is not clear when the VDF has steep variations or large discontinuities.

The aim of the present paper is to implement realistic intermolecular potentials in the fast spectral method (FSM), which is a promising numerical method for solving the BE deterministically[7,8,19,20]. By testing the proposed method, we also demonstrate the conditions in which the variable HS model can be adopted.

II. BOLTZMANN EQUATION

The state of a dilute monatomic gas is described by the VDF $f(t, x, v)$ of the molecular velocity $v = (v_1, v_2, v_3)$ at spatial location $x = (x_1, x_2, x_3)$ and time t. The evolution of f is governed by the BE:

$$\frac{\partial f}{\partial t} + v\frac{\partial f}{\partial x} = \mathcal{Q}(f, f_*), \tag{1}$$

where $v\partial/\partial x$ is the streaming operator, while $\mathcal{Q}$ is the BCO defined by

$$\mathcal{Q}(f, f_*) = \int_{\mathbb{R}^3}\int_{\mathbb{S}^2} |v - v_*|\sigma(\theta, |v - v_*|)[f(v'_*)f(v') - f(v_*)f(v)]d\Omega dv_*. \tag{2}$$

In the above equations, v, v_* are the molecular velocities before the binary collision, while v', v'_* are the corresponding post-collision velocities. Conservation of momentum and energy yields $v' = v + (|u|\Omega - u)/2$ and $v'_* = v_* - (|u|\Omega - u)/2$, where $u = v - v_*$ is the relative pre-collision velocity and Ω is a vector in the unit sphere $\mathbb{S}^2$ along the relative post-collision velocity $v' - v'_*$. The deflection angle θ between the pre- and post-collision relative velocities satisfies $\cos\theta = \Omega \cdot u/|u|$, with $0 \le \theta \le \pi$. Finally, $\sigma(\theta, |v - v_*|)$ is the DCS. For HS molecules with a molecular diameter d, it is $d^2/4$, while for a general intermolecular potential the dependence of σ on $|u|$ and θ is complicated and the numerical calculation of the DCS is necessary. Detailed information can be found in a recent publication[17].

In this paper, we consider the following (6-12) LJ potential as an example:

$$U'(\rho') = 4\epsilon \left[\left(\frac{d}{\rho'} \right)^{12} - \left(\frac{d}{\rho'} \right)^{6} \right], \tag{3}$$

where ρ' is the intermolecular distance, ϵ is a potential depth, and d is the distance at which the potential is zero. As the interaction range of the LJ potential is ostensibly infinity, the total cross-section, i.e. the integral of the DCS with respect to the deflection angle, is infinity too. In practice, however, a finite cutoff either in the deflection angle[16,18,21,22] or in the radial potential[10,17,23] is introduced.

A. Normalizations

For practical calculations, it is convenient to introduce dimensionless variables. Here, the spatial location is normalized by the characteristic length ℓ, temperature is normalized by T_0, velocity is normalized by the most probable molecular speed $v_m = \sqrt{2k_B T_0/m}$, time is normalized by ℓ/v_m, molecular number density is normalized by n_0, and the VDF is normalized by n_0/v_m^3, where k_B is the Boltzmann constant. Also, in the numerical evaluation of the DCS for the (6-12) LJ potential, the intermolecular distance ρ' is normalized by d. Therefore, the BE becomes

$$\frac{\partial f}{\partial t} + v\frac{\partial f}{\partial x} = \underbrace{n_0 d^2 \ell \int_{\mathbb{R}^3} \int_{\mathbb{S}^2} |u| \sigma(\theta, |u| v_m) f(v_*') f(v') d\Omega dv_*}_{\mathcal{Q}^+} - \nu(v) f, \tag{4}$$

where $\nu(v) = n_0 d^2 \ell \int_{\mathbb{R}^3} \int_{\mathbb{S}^2} |u| \sigma(\theta, |u| v_m) f(v_*) d\Omega dv_*$ is the collision frequency and $\sigma(\theta, |u| v_m)$ is exactly the same as the DCS $\sigma(\theta, E)$ in Ref.[17] with the dimensionless relative collision energy $E = u^2 k_B T_0/(2\epsilon)$.

The normalized density, flow velocity, and temperature are given by

$$n = \int f dv, \quad V = \frac{1}{n} \int v f dv, \quad T = \frac{2}{3n} \int |v - V|^2 f dv, \tag{5}$$

while the pressure tensor and heat flux, which are normalized by $n_0 k_B T_0$ and $n_0 k_B T_0 v_m$, respectively, are given by

$$P_{ij} = 2 \int (v_i - V_i)(v_j - V_j) f dv, \quad q_i = \int |v - V|^2 (v_i - V_i) f dv, \tag{6}$$

where $i, j = 1, 2, 3$.

B. Linearized Boltzmann equation

When the system state deviates only slightly from equilibrium, the BE (4) can be linearized. We express the VDF around the global equilibrium state as

$$f(t,x,v) = f_{eq}(v) + h(t,x,v), \quad f_{eq}(v) = \pi^{-3/2}\exp(-v^2), \tag{7}$$

where h is the deviation function satisfying $|h/f_{eq}| \ll 1$. The evolution of h is governed by the linearized BE:

$$\frac{\partial h}{\partial t} + v\frac{\partial h}{\partial x} = \mathcal{L}(h), \tag{8}$$

with the linearized BCO

$$\mathcal{L}(h) = \underbrace{n_0 d^2 \ell \int_{\mathbb{R}^3}\int_{\mathbb{S}^2} |u|\sigma[f_{eq}(v'_*)h(v') + h(v'_*)f_{eq}(v') - h(v_*)f_{eq}(v)]d\Omega dv_*}_{\mathcal{L}^+(h)} - \nu_{eq}h, \tag{9}$$

where $\nu_{eq} = n_0 d^2 \ell \int_{\mathbb{S}^2} |u|\sigma f_{eq}(v'_*)d\Omega dv_*$ is the equilibrium collision frequency.

III. FAST SPECTRAL METHOD FOR THE BOLTZMANN COLLISION OPERATOR

In this section, we focus on the numerical approximation of the BCO; the approximation of the linearized collision operator (9) can be performed according to the relation $\mathcal{L}(h) = \mathcal{Q}[f_{eq}(v), h(v_*)] + \mathcal{Q}[h(v), f_{eq}(v_*)]$. For simplicity, the coefficient $n_0 d^2 \ell$ is regarded as 1.

We rewrite the BCO in the Carleman representation as[7]

$$\mathcal{Q}(f, f_*) = 4\int_{\mathbb{R}^3}\int_{\mathbb{R}^3} \sigma\delta(y\cdot z)[f(v+z)f(v+y) - f(v+y+z)f(v)]dydz, \tag{10}$$

where δ is Dirac's delta function, and the DCS becomes

$$\sigma(\theta, |u|v_m) = \sigma\left(2\arctan\frac{|y|}{|z|}, v_m\sqrt{|y|^2 + |z^2|}\right) \equiv \sigma'(|y|, |z|). \tag{11}$$

The VDF is periodized on the truncated velocity domain $\mathcal{D}_L = [-L, L]^3$. For simplicity, we adopt uniform discretization in velocity space: $v_k(j_k) = 2j_k L/N_k$ with $k = 1, 2, 3$, where $j_k \in [-N_k/2, -N_k/2+1, \cdots, N_k/2-1]$ and N_k is the number of velocity grid points in the k-th velocity direction, although in the simulation of highly rarefied gas flows the velocity space would be better discretized non-uniformly[8,20]. The VDF is approximated by a truncated Fourier series: $f(v) = \sum_{j=-(N_1,N_2,N_3)/2}^{(N_1,N_2,N_3)/2-1} \hat{f}_j \exp(i\xi_j \cdot v)$, where

$\hat{f}_j = \int_{\mathcal{D}_L} f(v)\exp(-i\xi_j\cdot v)dv/(2L)^3$, $j=(j_1,j_2,j_3)$ is the Fourier spectrum of the VDF, i is the imaginary unit, and $\xi_j = j\pi/L$ are the frequency components.

Equation (10) is truncated to $\mathcal{Q}(f,f_*) = 4\int_{\mathcal{B}_R}\int_{\mathcal{B}_R}\sigma'(|y|,|z|)\delta(y\cdot z)[f(v+z)f(v+y) - f(v+y+z)f(v)]dydz$, where $R\geq\sqrt{2}S$, and $\mathcal{B}_S$ (a sphere of radius S centered on the origin) is the support of the VDF[19]. Our numerical experience suggests that $R = 2\sqrt{2}L/(2+\sqrt{2})$ is a good choice[7,8]. The truncated BCO is also expanded by the Fourier series, where its j-th Fourier mode is related to the Fourier coefficient $\hat{f}$ of the VDF as follows:

$$\widehat{\mathcal{Q}}_j = \frac{1}{(2L)^3}\int_{\mathcal{D}_L}\mathcal{Q}(v)\exp(-i\xi_j\cdot v)dv = \sum_{\substack{l+m=j\\ l,m=-(N_1,N_2,N_3)/2}}^{(N_1,N_2,N_3)/2-1}\hat{f}_l\hat{f}_m[\beta(l,m)-\beta(m,m)], \tag{12}$$

where $l=(l_1,l_2,l_3)$, $m=(m_1,m_2,m_3)$, and the kernel mode $\beta(l,m)$ is

$$\beta(l,m) = \int\int\delta(e\cdot e')\left[\int_{-R}^{R}\int_{-R}^{R}|\rho\rho'|\sigma'(|\rho|,|\rho'|)\exp(i\rho\xi_l\cdot e + i\rho'\xi_m\cdot e')d\rho d\rho'\right]de'de, \tag{13}$$

with e, e' being the vectors in the unit sphere $\mathbb{S}^2$.

The integration with respect to ρ in Eq. (13) can be approximated by a numerical quadrature. Suppose ρ_r and ω_r ($r=1,2,\cdots,M_r$) are the abscissas and weights of a quadrature for ρ in the region $[0,R]$, Eq. (13) becomes $\beta(l,m) = \sum_r\omega_r\int\phi(\rho_r,\xi_l\cdot e)\int\delta(e\cdot e')\psi(\rho_r,\xi_m\cdot e')de'de$, where $\psi(\rho_r,s) = 2\int_0^R\rho'\sigma'(\rho_r,\rho')\cos(\rho' s)d\rho'$ and $\phi(\rho_r,s) = 2\rho_r\cos(\rho_r s)$. Following the steps from Eq. (34) to Eq. (39) in Ref.[7], the final expression for the kernel mode is

$$\beta(l,m) = 4\sum_{p,q,r=1}^{M,M,M_r}\omega_p\omega_q\omega_r\phi(\rho_r,\xi_l\cdot e_{\theta_p,\varphi_q})\psi'\left(\rho_r,\sqrt{|\xi_m|^2-|\xi_m\cdot e_{\theta_p,\varphi_q}|^2}\right)\sin\theta_p, \tag{14}$$

where θ_p (φ_q) and ω_p (ω_q) are the p (q)-th point and weight in the Gauss-Legendre quadrature with $\theta,\varphi\in[0,\pi]$, and

$$\psi'(\rho_r,s) = \int_0^\pi\psi(\rho_r,s\cos\theta_2)d\theta_2 = 2\pi\int_0^R\rho'\sigma'(\rho_r,\rho')J_0(\rho' s)d\rho', \tag{15}$$

with J_0 being the zeroth-order Bessel function of first kind.

Thus, combining Eqs. (12) and (14), $\widehat{\mathcal{Q}}$ can be calculated through FFT-based convolution, with a computational cost of $O(M^2M_rN^3\log N)$. Since M and M_r can be far smaller than N, the FSM proposed here is faster than conventional spectral methods that have a cost of $O(N^6)$. Note that in our previous works[7,8], a special form of DCS was proposed to approximate the DCS for the LJ potential, and since that special DCS can be decomposed

into the form of $\sigma'(|y|,|z|) = \sigma'_1(|y|)\sigma'_2(|z|)$, the integration with respect to ρ in Eq. (13) can be expressed analytically, resulting in a computational cost of $O(M^2N^3 \log N)$ for the BCO. Here, for general DCSs, one must approximate the integration with respect to ρ or ρ' by a numerical quadrature to get a computational gain; and this approximation extends the applicability of the FSM.

Finally, when $\widehat{\mathcal{Q}}$ is obtained, the BCO is then calculated through $\mathcal{Q}(v) = \sum \widehat{\mathcal{Q}}_j \exp(i\xi_j \cdot v)$. As with the FSM that was developed for specific forms of DCS, this new FSM conserves mass, while momentum and energy are conserved at spectral accuracy.

To obtain the kernel mode $\beta(l,m)$, ρ is first discretized and then $\psi'(\rho_r, s)$ is calculated. For the (6-12) LJ potential, for each relative collision energy E, the DCS is a continuous function of the deflection angle at $E = u^2 k_B T_0/(2\epsilon) = (\rho_r^2 + \rho'^2)k_B T_0/(2\epsilon) \lesssim 1$ and has one discontinuous point at $E > 1$[17]. Therefore, the integration region $0 \le \rho \le R$ is divided into two regions: the first region $[0, \sqrt{2\epsilon/k_B T_0}]$ is divided into 9 uniform sections, while the second region $[\sqrt{2\epsilon/k_B T_0}, R]$ is discretized according to the Gauss-Legendre quadrature of order 7. So the number of points in the discretization of ρ is $M_r = 16$.

When ρ_r is determined, the integral given by Eq. (15) is calculated numerically, where $s \in [0, \max(\sqrt{3}\xi)]$ is uniformly discretized into 8000 sections. The key part is to calculate the DCS $\sigma'(\rho_r, \rho')$. We first check the continuity of the DCS as ρ' goes from 0 to R. If $\sigma'(\rho_r, \rho')$ is continuous, then Eq. (15) is approximated by the Gauss-Legendre quadrature of order 120. Otherwise, suppose $\sigma'(\rho_r, \rho')$ is discontinuous at $\rho' = \rho'_d$, then the region $\rho' \in [0, \rho'_d)$ is discretized non-uniformly by 60 points, with most of the points located near ρ'_d, while the remaining region $\rho' \in [\rho'_d, R]$ is approximated by the Gauss-Legendre quadrature of order 60. In the numerical integration of ψ', a DCS with deflection angle less than 0.05 radians is neglected. Finally, when $\psi'(\rho_r, s)$ is obtained, $\psi'\left(\rho_r, \sqrt{|\xi_m|^2 - |\xi_m \cdot e_{\theta_p,\varphi_q}|^2}\right)$ is calculated through cubic interpolation.

IV. NUMERICAL ACCURACY

To assess the accuracy of the proposed FSM, we run two test cases. The first is the calculation of the transport coefficients of five noble gases, and the second is the calculation of mass/heat flow rates in Poiseuille/thermal transpiration flows. We compare our results with those from the variational method[24] and the discrete velocity method[10,17].

A. Transport coefficients

The shear viscosity μ' and thermal conductivity κ' are calculated as

$$\begin{aligned}\mu' =& \frac{m v_m}{d^2}\int h_\mu(v) v_1 v_2 dv \equiv \frac{m v_m}{d^2}\mu,\\ \kappa' =& \frac{k_B v_m}{d^2}\int h_\kappa(v) v_1 \left(v^2-\frac{5}{2}\right) dv \equiv \frac{k_B v_m}{d^2}\kappa,\end{aligned} \tag{16}$$

where μ and κ are the reduced shear viscosity and thermal conductivity, respectively. The two functions $h_\mu(v)$ and $h_\kappa(v)$ satisfy the following integral equations:

$$\begin{aligned}&\mathcal{L}(h_\mu) = -2 f_{eq} v_1 v_2,\\ &\mathcal{L}(h_\kappa) = -f_{eq} v_1 \left(v^2-\frac{5}{2}\right), \quad \text{and} \int h_\kappa v_1 dv = 0.\end{aligned} \tag{17}$$

To find h_μ and h_κ, Eq. (17) is solved by the following iterative scheme (with k the iteration step):

$$\begin{aligned}h_\mu^{(k+1)} =& \frac{\mathcal{L}^+(h_\mu^{(k)}) + 2 f_{eq} v_1 v_2}{\nu_{eq}},\\ \widetilde{h}_\kappa^{(k+1)} =& \frac{\mathcal{L}^+(h_\kappa^{(k)}) + f_{eq} v_1 \left(v^2-\frac{5}{2}\right)}{\nu_{eq}}, \quad h_\kappa^{(k+1)} = \widetilde{h}_\kappa^{(k+1)} - 2 f_{eq} v_1 \int \widetilde{h}_\kappa^{(k+1)} v_1 dv.\end{aligned} \tag{18}$$

The molecular velocity space $[-6,6]^3$ is discretized by $64\times 24\times 24$ uniform grid points, while $M=8$ is chosen in the discretization of the solid angle, see Eq. (14). Potential depths for the five noble gases are adopted from Ref.[17]: $k_B T_0/\epsilon$ are 29.35, 8.403, 2.419, 1.579, and 1.310 for He, Ne, Ar, Kr, and Xe, respectively, at $T_0 = 300$ K. The iterations of Eq. (18) are terminated when the relative difference in the transport coefficient between two consecutive iterative steps is less than 10^{-6}. When the DCS is obtained, our FSM needs less than 30 seconds to obtain one transport coefficient, through a Matlab program running on an Intel Xeon 3.3 GHz CPU. Numerical results for the transport coefficients are summarized in Table I, where we see that the difference between the FSM results and those from the variational and discrete velocity methods[17] is small: the maximum relative error is less than 0.5%.

It is interesting to see how the inverse Schmidt number, defined as the ratio of mass diffusivity to momentum diffusivity (viscosity), changes between the various noble gases. Here, the mass-diffusion coefficient is calculated as

$$D' = \frac{v_m}{n d^2}\int h(v) v_1 dv \equiv \frac{v_m}{n d^2} D, \tag{19}$$

TABLE I. Comparisons of reduced transport coefficients obtained from the FSM with those from the variational method with third-order Chapman-Cowling approximation[24] and the discrete velocity method[17].

	Reduced shear viscosity μ			Reduced thermal conductivity κ		
Gas	Variational method $\mu^{(3)}$	Discrete velocity method	FSM	Variational method $\kappa^{(3)}$	Discrete velocity method	FSM
He	0.17873	0.1787	0.1789	0.67320	0.6740	0.6742
Ne	0.14878	0.1480	0.1486	0.56018	0.5600	0.5596
Ar	0.11314	0.1130	0.1132	0.42479	0.4260	0.4251
Kr	0.09690	0.0968	0.0967	0.36349	0.3645	0.3629
Xe	0.08928	0.0892	0.0894	0.33485	0.3358	0.3354

TABLE II. Comparisons of inverse Schmidt number (nmD'/μ') obtained from the FSM with those from the variational method with first-order Chapman-Cowling approximation[24,25].

Gas	HS	He	Ne	Ar	Kr	Xe
Variational method	1.2	1.32	1.35	1.33	1.29	1.33
FSM	1.2128	1.3541	1.3321	1.3139	1.3199	1.3237
Relative error	1.1%	2.2%	1.5%	1.5%	2.3%	0.8%

where D is the reduced mass-diffusion coefficient and $h_D(v)$ satisfies the following equation

$$\underbrace{n_0 d^2 \ell \int_{\mathbb{R}^3}\int_{\mathbb{S}^2} |u|\sigma[f_{eq}(v_*')h(v') - h(v_*')f_{eq}(v') + h(v_*)f_{eq}(v)]d\Omega dv_*}_{\mathcal{L}_D^+(h)} - \nu_{eq}h = -2f_{eq}v_1. \quad (20)$$

Similar to Eq. (17), Eq. (20) is solved in the following iterative scheme:

$$h^{(k+1)} = \frac{\mathcal{L}_D^+(h^{(k)}) + 2f_{eq}v_1}{\nu_{eq}}. \quad (21)$$

Numerical results from the FSM for noble gases and the HS gas at $T = 300$ K are shown in Table II, together with those from the variational method[1,25]. We find that the relative error between the two methods is about 2%.

TABLE III. Mass flow rate G_P in the Poiseuille flow of various gases between parallel infinite plates. The data in columns denoted by SB are from Ref[10].

	He		Ne		Ar		Kr		Xe	
δ	FSM	SB	FSM	SB	FSM	SB	FSM	SB	FSM	SB
0.010	2.713	2.668	2.607	2.581	2.535	2.502	2.538	2.495	2.547	2.497
0.020	2.432	2.424	2.362	2.358	2.292	2.280	2.286	2.269	2.290	2.270
0.025	2.348	2.345	2.289	2.287	2.219	2.211	2.211	2.199	2.214	2.199
0.040	2.180	2.182	2.141	2.140	2.076	2.072	2.063	2.058	2.064	2.057
0.050	2.105	2.107	2.074	2.073	2.011	2.009	1.998	1.995	1.998	1.993
0.100	1.892	1.893	1.879	1.876	1.829	1.830	1.815	1.816	1.813	1.813
0.200	1.713	1.715	1.708	1.707	1.677	1.679	1.666	1.668	1.663	1.665
0.250	1.665	1.667	1.661	1.661	1.636	1.637	1.626	1.628	1.624	1.625
0.400	1.581	1.582	1.579	1.580	1.564	1.566	1.558	1.559	1.556	1.557
0.500	1.550	1.552	1.549	1.550	1.539	1.540	1.534	1.535	1.532	1.533
1.000	1.505	1.507	1.505	1.508	1.505	1.507	1.505	1.507	1.505	1.507
1.600	1.532	1.534	1.533	1.536	1.537	1.540	1.540	1.543	1.541	1.544
2.000	1.568	1.570	1.568	1.572	1.575	1.578	1.579	1.582	1.580	1.583
2.500	1.622	1.624	1.623	1.626	1.630	1.634	1.636	1.639	1.637	1.641
4.000	1.817	1.819	1.818	1.822	1.828	1.833	1.835	1.839	1.838	1.842
5.000	1.960	1.963	1.961	1.966	1.972	1.978	1.980	1.985	1.983	1.988
10.00	2.732	2.740	2.732	2.743	2.743	2.756	2.752	2.764	2.756	2.768

B. Poiseuille and thermal transpiration flows

We now consider a monatomic gas confined between two parallel infinite plates located at $x_2 = \pm\ell/2$. In Poiseuille flow, the wall temperature is fixed at T_0, and a uniform pressure gradient is imposed on the gas in the x_3 direction: the pressure is given by $n_0 k_B T_0(1 + \xi_P x_3/\ell)$ with $|\xi_P| \ll 1$. In thermal transpiration flow, the pressure is fixed at $n_0 k_B T_0$, but a temperature gradient is imposed on both walls: the wall temperature is $T = T_0(1 + \xi_T x_3/\ell)$ with $|\xi_T| \ll 1$. The VDF is expressed as $f = f_{eq} + \xi_P(x_3 f_{eq} + h_P) + \xi_T[x_3 f_{eq}(v^2 - 5/2) + h_T]$,

TABLE IV. Heat flow rates Q_P and Q_T in Poiseuille flow of various gases between parallel infinite plates. The data in columns denoted by SB are results from Ref[10].

	He		Ne		Ar		Kr		Xe	
δ	FSM	SB	FSM	SB	FSM	SB	FSM	SB	FSM	SB
0.010	1.152	1.142	1.070	1.103	1.057	1.055	1.065	1.053	1.072	1.056
0.020	1.021	1.027	0.961	0.990	0.930	0.937	0.933	0.933	0.938	0.935
0.025	0.981	0.989	0.929	0.954	0.893	0.900	0.894	0.895	0.898	0.897
0.040	0.900	0.909	0.862	0.878	0.819	0.824	0.815	0.818	0.818	0.819
0.050	0.863	0.870	0.831	0.843	0.785	0.790	0.780	0.782	0.782	0.783
0.100	0.749	0.751	0.732	0.734	0.688	0.689	0.679	0.680	0.679	0.679
0.200	0.637	0.637	0.629	0.627	0.596	0.595	0.586	0.585	0.584	0.583
0.250	0.601	0.601	0.595	0.593	0.566	0.565	0.557	0.556	0.555	0.554
0.400	0.526	0.526	0.523	0.521	0.504	0.503	0.497	0.495	0.495	0.493
0.500	0.491	0.491	0.489	0.487	0.474	0.473	0.468	0.467	0.466	0.465
1.000	0.385	0.385	0.384	0.383	0.380	0.379	0.378	0.377	0.377	0.376
1.600	0.315	0.315	0.315	0.314	0.315	0.315	0.316	0.315	0.315	0.315
2.000	0.282	0.282	0.283	0.282	0.285	0.284	0.286	0.285	0.286	0.286
2.500	0.251	0.251	0.251	0.251	0.254	0.254	0.256	0.256	0.257	0.256
4.000	0.188	0.188	0.189	0.189	0.193	0.193	0.196	0.196	0.197	0.197
5.000	0.161	0.161	0.162	0.162	0.166	0.166	0.169	0.169	0.170	0.170
10.00	0.093	0.093	0.093	0.093	0.097	0.097	0.099	0.099	0.100	0.100

and the perturbation functions h_P and h_T satisfy

$$\begin{aligned} v_2 \frac{\partial h_\alpha}{\partial x_2} =& \mathcal{L}(h_\alpha) + S_\alpha, \qquad \alpha = P,\ T, \\ S_P =& -v_3 f_{eq}, \quad S_T = -v_3 \left(v^2 - \frac{5}{2} \right) f_{eq}, \end{aligned} \tag{22}$$

where subscripts P and T stand for the Poiseuille and thermal transpiration flows, respectively.

We assume a diffuse gas-wall interaction, so h_α is zero for gas molecules entering the computational domain. Due to symmetry, only half of the spatial domain is considered: the normalized x_2 varies from $-1/2$ to 0. The dimensionless mass and heat flow rates are

TABLE V. Heat flow rates Q_P and Q_T in thermal transpiration flow of various gases between parallel infinite plates. The data in columns denoted by SB are results from Ref[10].

	He		Ne		Ar		Kr		Xe	
δ	FSM	SB	FSM	SB	FSM	SB	FSM	SB	FSM	SB
0.010	5.946	5.879	5.761	5.684	5.585	5.512	5.589	5.496	5.606	5.500
0.020	5.263	5.263	5.139	5.121	4.983	4.958	4.969	4.934	4.977	4.935
0.025	5.051	5.059	4.946	4.936	4.796	4.779	4.777	4.754	4.783	4.754
0.040	4.614	4.626	4.544	4.542	4.409	4.404	4.384	4.376	4.385	4.373
0.050	4.411	4.421	4.354	4.353	4.228	4.225	4.201	4.197	4.199	4.193
0.100	3.789	3.792	3.761	3.761	3.665	3.669	3.637	3.641	3.633	3.635
0.200	3.172	3.174	3.159	3.162	3.096	3.103	3.073	3.080	3.068	3.074
0.250	2.974	2.977	2.964	2.968	2.911	2.918	2.890	2.897	2.884	2.891
0.400	2.559	2.562	2.553	2.560	2.517	2.525	2.500	2.508	2.495	2.502
0.500	2.364	2.367	2.359	2.366	2.329	2.337	2.314	2.322	2.309	2.317
1.000	1.767	1.770	1.765	1.771	1.748	1.756	1.738	1.745	1.735	1.741
1.600	1.383	1.385	1.382	1.387	1.370	1.377	1.363	1.369	1.361	1.366
2.000	1.212	1.213	1.210	1.216	1.201	1.207	1.195	1.201	1.193	1.198
2.500	1.050	1.051	1.049	1.053	1.042	1.046	1.037	1.041	1.035	1.039
4.000	0.754	0.750	0.748	0.752	0.744	0.747	0.741	0.744	0.740	0.743
5.000	0.628	0.629	0.627	0.630	0.624	0.627	0.622	0.625	0.621	0.624
10.00	0.345	0.345	0.345	0.346	0.343	0.345	0.343	0.344	0.342	0.344

$G_P = -4\int_{-1/2}^{0} V_P dx_2$, $G_T = 4\int_{-1/2}^{0} V_T dx_2$, $Q_P = 4\int_{-1/2}^{0} q_P dx_2$, and $Q_T = -4\int_{-1/2}^{0} q_T dx_2$, where the gas velocity is $V_\alpha = \int v_3 h_\alpha dv$ and the heat flux is $q_\alpha = \int v_3 \left(v^2 - \frac{5}{2}\right) h_\alpha dv$. These flow rates are a function of the rarefaction parameter, defined as

$$\delta = \frac{n_0 k_B T_0 \ell}{\mu' v_m}. \tag{23}$$

In the numerical simulations, the spatial domain $-0.5 \le x_2 \le 0$ is divided into 100 non-uniform sections, with most of the discrete points placed near the wall: $x_2 = (10 - 15s + 6s^2)s^3 - 0.5$, where $s = (0, 1, \cdots, 100)/200$. Because of the symmetry and smoothness of the VDF in the v_1 and v_3 directions, $N_1, N_3 = 12$ uniform grids are used in the $v_1(>$

0) and $v_3(>0)$ directions, where the maximum molecular velocity is at $L = 6$. In the discretization of v_2, $N_2 = 128$ non-uniform grid points are used: $v_2 = 4(-N_2+1, -N_2+3, \cdots, N_2-1)^3/(N_2-1)^3$, with most of the grid points located near $v_2 \sim 0$. This choice is necessary at small values of the rarefaction parameter, as the VDF over-concentrates in this region[21]. The number of frequency components in the ξ_1 and ξ_3 directions are 24×24, while there are 64 frequency components in the ξ_2 direction. For more details, see Ref.[8].

We use the following iterative scheme to solve Eq. (22):

$$v_2 \frac{\partial h_\alpha^{(k+1)}}{\partial x_2} + \nu_{eq}(v) h_\alpha^{(k+1)} = \mathcal{L}^+(h_\alpha^{(k)}) + S_\alpha, \tag{24}$$

where k is the iteration step and the spatial derivative is approximated by a second-order upwind finite difference. Iterations are terminated when the relative difference in mass and heat flow rates between two consecutive steps is less than 10^{-6}.

Tables III, IV, and V compare our numerical results for G_P, G_T, and Q_T with those by Sharipov and Bertoldo[10]. The mass flow rate G_T is not shown, as $G_T = Q_P$ according to the Onsager-Casimir relation, and our numerical results show that the relative difference between G_T and Q_P is less than 0.2%. For $\delta \geq 0.025$, the difference between our results and those of Sharipov and Bertoldo is $\lesssim 1\%$, which increases to about 2% at $\delta = 0.01$. These differences are small, as the numerical accuracy of the discrete velocity method itself is about 0.8%.[10]

V. APPLICATIONS

We now apply the FSM for the BE with LJ potentials to solve Couette and Fourier flows between two parallel plates. The five noble gases He, Ne, Ar, Kr, and Xe, as well as the variable HS gas, are considered and the effect of the intermolecular potential on the flow properties is investigated. Note that for the variable HS gas, the DCS is proportional to $|u|^{1-2\omega}$, where ω is the viscosity index (i.e. the gas viscosity is proportional to T^ω). For the HS gas, $\omega = 0.5$, while for He and Xe at $T = 300$ K, ω=0.66 and 0.85, respectively.

A. Planar Fourier flow

The geometry is the same as that of the Poiseuille flow in Section IV B, except that the plate at $x_2 = -1/2$ has a temperature $T_0 - \Delta T/2$, while the plate at $x_2 = 1/2$ has a

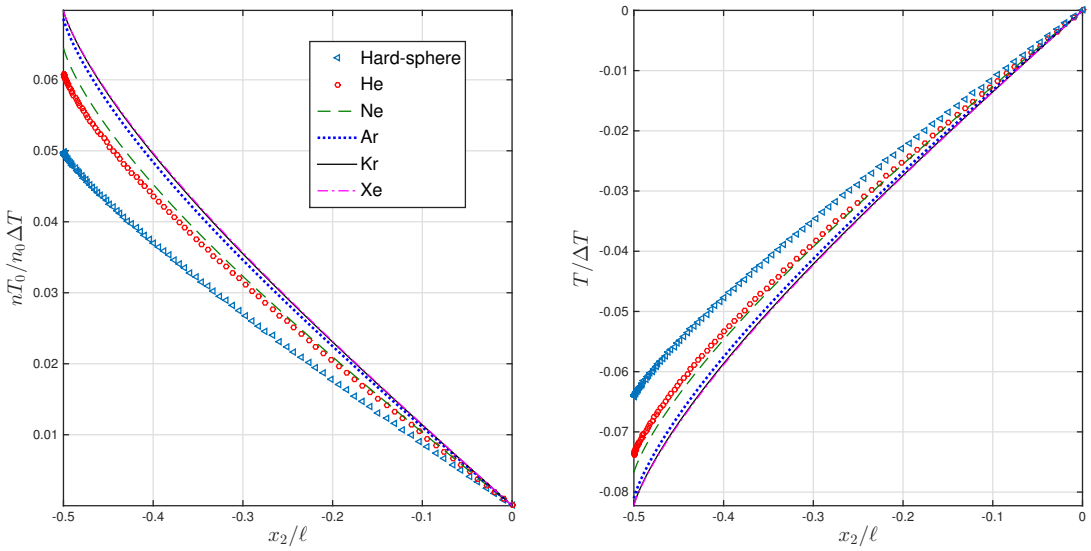

FIG. 1. Normalized density and temperature half-channel profiles in the linearized Fourier flow of various gases between two parallel plates with $\delta = 0.1$.

temperature $T_0 + \Delta T/2$. Also, there is no pressure gradient along the x_1 and x_3 directions. We first assume that the temperature difference ΔT is negligible compared to T_0, so that the BE (4) can be linearized to Eq. (8) by expressing the VDF as $f = f_{eq} + h\Delta T/T_0$.

The spatial region $-1/2 \le x_2 \le 0$ is discretized by 100 non-uniform grid points, with most of the grid points located near the wall. The three-dimensional molecular velocity domain $[-6, 6]^3$ is discretized by $32 \times 128 \times 32$ grid points, and the number of frequency components is $32 \times 48 \times 32$. Assuming diffuse gas-wall interaction, the boundary condition reads

$$h(v, x_2 = -0.5) = \left[1 - \frac{1}{2}v^2 - 2\sqrt{\pi}\int_{v_2<0} v_2 h(v, x_2 = -0.5)dv\right] f_{eq}, \quad \text{at } v_2 > 0, \tag{25}$$

while at $x_2 = 0$, symmetry leads to $h(v_1, v_2, v_3) = -h(v_1, -v_2, v_3)$ when $v_2 < 0$. The iterative scheme $v_2 \partial h^{(k+1)}/\partial x_2 + \nu_{eq}(v) h^{(k+1)} = \mathcal{L}^+(h^{(k)})$ is used, and the iterations are terminated when the maximum relative difference in the density $n = \int h dv$, temperature $T = 2\int hv^2 dv/3 - n$, and heat flux $q_2 = \int hv^2 v_2 dv$ between two consecutive steps is less than 10^{-5}.

Typical density and temperature profiles are shown in Fig. 1 for a rarefaction parameter of $\delta = 0.1$ and $T_0 = 300$ K. Although they have the same rarefaction parameter, the macroscopic properties of the six gases are quite different. The differences are summarized

TABLE VI. Normalized gas density (n) and temperature (T) at the plate located at $x_2 = -0.5$, and the heat flux (q_2) in the linearized Fourier flow at $T_0 = 300$ K.

	$\delta = 0.1$			$\delta = 1$			$\delta = 10$		
	n	$-T$	q_2	n	$-T$	q_2	n	$-T$	q_2
HS	0.050	0.064	0.536	0.176	0.206	0.406	0.392	0.405	0.137
He	0.061	0.074	0.534	0.184	0.214	0.403	0.395	0.408	0.136
Ne	0.065	0.077	0.533	0.187	0.216	0.402	0.396	0.408	0.136
Ar	0.069	0.081	0.531	0.193	0.221	0.398	0.398	0.410	0.135
Kr	0.070	0.080	0.530	0.196	0.224	0.397	0.398	0.411	0.135
Xe	0.070	0.080	0.530	0.196	0.224	0.396	0.399	0.411	0.134

in Table VI for $\delta = 0.1$, 1, and 10. At the wall, when $\delta = 0.1$, the relative difference in density between He and the HS gas is 22%. This difference between LJ and HS potentials increases as $k_B T_0/\epsilon$ decreases: the density of Xe at the wall is 40% larger than that of the HS gas. For the temperature, the largest difference between the noble gases and the HS gas reaches 25%. As δ increases, relative differences in the densities and the temperature decrease: when $\delta = 1$, relative differences in the density and temperature of the HS gas and Xe at the wall are reduced to 11.4% and 8.7%, respectively, while they are 1.8% and 1.5% by $\delta = 10$. As δ further increases, the hydrodynamic flow regime is reached and there is no difference between the various gases. Interestingly, the differences in the heat flux between the various gases are small and first increase and then decrease with δ. At $\delta = 0.1$, the relative heat flux difference between the HS gas and Xe is only 1.1%; this increases to 2.5% at $\delta = 1$, and then decreases to 2% by $\delta = 10$. Therefore, if only the heat flux is of interest, the HS gas model can be safely used, with a numerical error of less than two percent.

We also consider the variable HS gas with viscosity index $\omega = 0.66$ and 0.85, at $\delta = 0.1$: at $x_2 = -0.5$, the gas densities are 0.051 and 0.058, respectively. When compared to that of He and Xe, we find that the variable HS model does not produce significant improvement on the HS model, i.e. there are still about 20% and 14% relative differences in gas density and temperature between the variable HS model and the LJ potential, respectively.

We then consider the nonlinear heat transfer between the two parallel plates by reducing the temperature of the plate at $x_2 = -0.5$ to $T_0/2$, while that at $x_2 = 0.5$ remains at

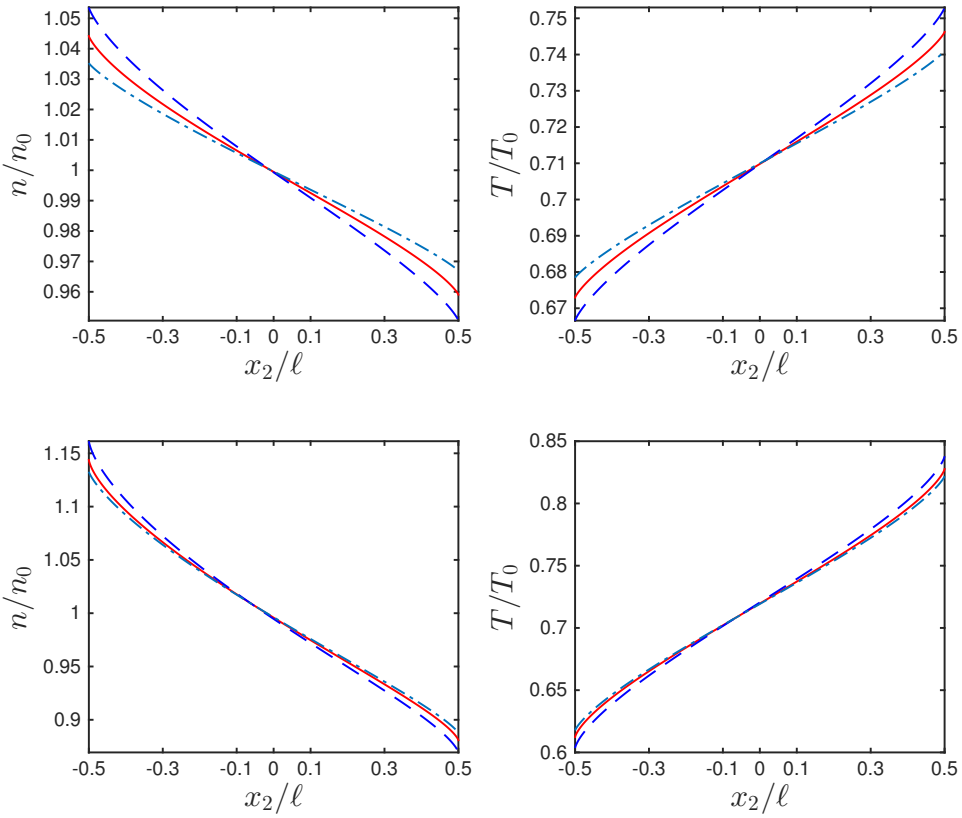

FIG. 2. Density and temperature profiles in the nonlinear Fourier flow between two parallel plates when $\delta = 0.1$ (top row) and $\delta = 1$ (bottom row). Dash-dotted lines: HS gas; Solid lines: He; Dashed lines: Kr.

$T_0 = 300$ K. The BE (4) is solved in an iterative manner:

$$v_2 \frac{\partial f^{(k+1)}}{\partial x_2} + \nu(v) f^{(k+1)} = \mathcal{Q}^+(f^{(k)}), \tag{26}$$

with the following diffuse boundary conditions

$$\begin{aligned} f(v, x_2 = -0.5) =& \frac{n_{w1}}{(\pi T_0/2)^{3/2}} \exp\left(-\frac{2v^2}{T_0}\right), \quad \text{for } v_2 > 0, \\ f(v, x_2 = 0.5) =& \frac{n_{w2}}{(\pi T_0)^{3/2}} \exp\left(-\frac{v^2}{T_0}\right), \quad \text{for } v_2 < 0, \end{aligned} \tag{27}$$

where $n_{w1} = -2\sqrt{2\pi/T_0} \int_{v_2<0} f v_2 dv$ and $n_{w2} = 2\sqrt{\pi/T_0} \int_{v_2>0} f v_2 dv$.

We compare He and Kr with the HS gas, as the results for Xe are very close to Kr, while the results for Ne and Ar lie between those for He and Kr. Figure 2 shows the density and temperature profiles when $\delta = 0.1$ and 1. As in the linear case, the variations in the density

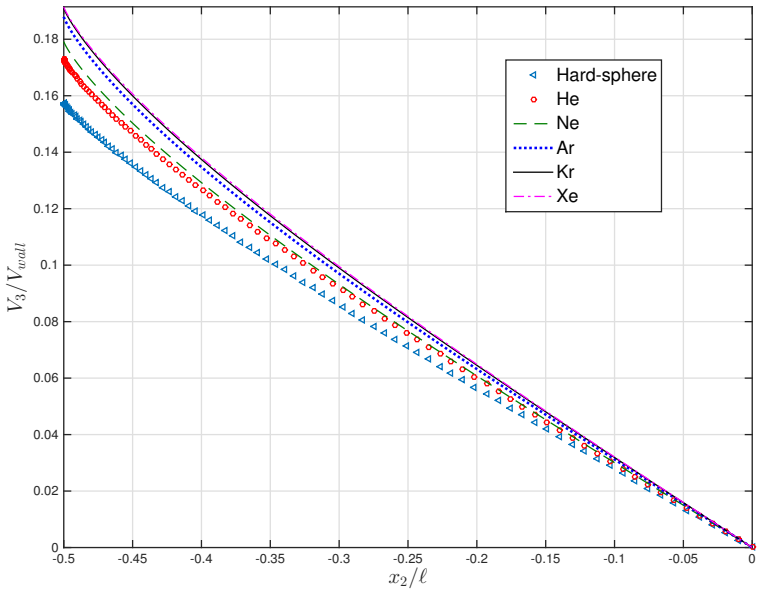

FIG. 3. Velocity half-channel profiles in the linearized planar Couette flow of various gases when $\delta = 0.1$.

and temperature of He and Kr are steeper than the HS gas, and as δ increases the differences between He, Kr, and the HS gas decrease. The heat flux in the HS gas, He, and Xe are, respectively, 0.223, 0.221, and 0.219 when $\delta = 0.1$; 0.170, 0.168, and 0.159 when $\delta = 1$; and 0.059, 0.056, 0.052 when $\delta = 10$. Unlike the heat transfer in the linearized case, here the difference in the heat flux between the HS gas and Xe reaches about 7% at $\delta = 1$ and 13% by $\delta = 10$. This is due to the HS gas having a higher thermal conductivity near the plate at $x_2 = -\ell/2$.

B. Planar Couette flow

The geometry is the same as that for the Poiseuille flow in Section IV B, except that the plate at $x_2 = -\ell/2$ moves in the x_3 direction with a speed V_{wall}, while the other plate moves in the opposite direction with the same speed. Also, there is no pressure gradient along the x_1 and x_3 directions. We first consider the case when the wall speed is far smaller than the most probable molecular speed v_m, hence the BE can be linearized to Eq. (8) by expressing the VDF as $f = f_{eq} + hV_{wall}/v_m$. The numerical method is then exactly as that for Fourier flow, except that the diffuse gas-wall boundary condition becomes $h(v, x_2 = -0.5) = 2v_3 f_{eq}$

TABLE VII. Velocity V_3 at the plate and the shear stress P_{23} in the linearized Couette flow at $T_0 = 300$ K.

	$\delta = 0.1$		$\delta = 1$		$\delta = 10$	
	V_3	P_{23}	V_3	P_{23}	V_3	P_{23}
HS	0.157	1.042	0.502	0.681	0.881	0.167
He	0.173	1.038	0.511	0.678	0.882	0.167
Ne	0.179	1.037	0.515	0.677	0.883	0.167
Ar	0.188	1.033	0.522	0.674	0.884	0.166
Kr	0.191	1.031	0.525	0.671	0.885	0.166
Xe	0.192	1.031	0.526	0.670	0.885	0.166

for $v_2 > 0$, and $h(v_1, v_2, v_3, x_2 = 0) = h(v_1, -v_2, -v_3, x_2 = 0)$ for $v_2 < 0$ due to symmetry. We are interested in the gas velocity and the shear stress. The velocity, which is normalized by the wall speed, is $V_3 = \int h v_3 dv$; the shear stress, which is normalized by $n_0 k_B T_0 V_{wall}/v_m$, is $P_{23} = 2\int h v_2 v_3 dv$.

Figure 3 depicts the typical velocity profiles when $\delta = 0.1$, where the influence of the molecular potential is clearly seen. Table VII lists the gas velocity at the wall and the shear stress for the different gases when $\delta = 0.1$, 1, and 10. As δ increases, the differences in the velocity profiles of the six gases decrease. For instance, the relative difference between the HS gas and Xe decreases from 22.3% when $\delta = 0.1$, to 4.5% at $\delta = 1$, and to 0.5% by $\delta = 10$. Similar to heat fluxes in the Fourier flows, the relative differences in shear stress between the various gases in Couette flow are small, and first increase and then decrease with δ.

We also consider the variable HS gas with viscosity index $\omega = 0.85$ at $\delta = 0.1$, and compare the gas velocity at the plate to that Xe. As in the linearized Fourier flow, the variable HS model does not produce significant improvement when compared to the HS model, as the velocity at the plate is 0.167 for $\omega = 0.85$, so that for Xe the relative difference between the variable HS model and LJ potential is 15%.

Finally, we consider nonlinear Couette flow, with a wall speed $V_{wall} = v_m$. The wall temperature is set to be $T_0/2$. The iterative scheme is the same as in the nonlinear Fourier flow case, see Eq. (26). The boundary condition is:

$$f(v, x_2 = -0.5) = \frac{n_w}{(\pi T_0/2)^{3/2}} \exp\left(-2\frac{v_1^2 + v_2^2 + (v_3 - 1)^2}{T_0}\right), \quad \text{for } v_2 > 0, \tag{28}$$

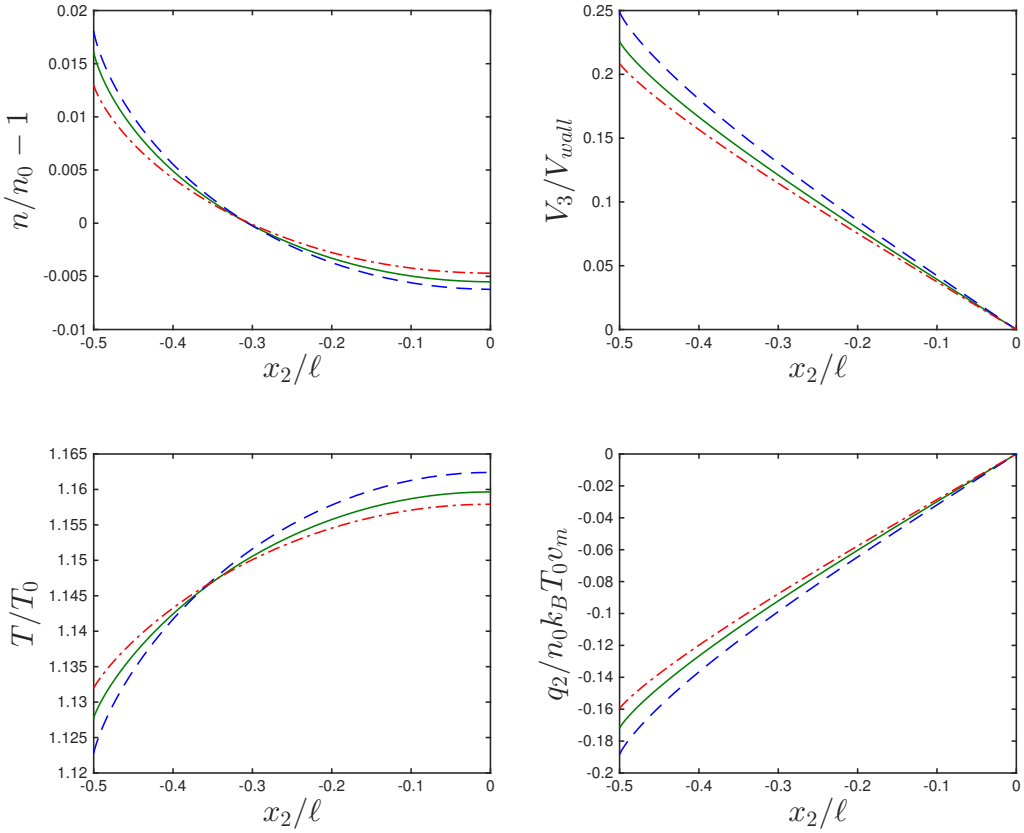

FIG. 4. Half-channel profiles of the density, velocity, temperature, and heat flux in nonlinear Couette flow at $\delta = 0.1$. Dash-dotted lines: HS gas; Solid lines: He; Dashed lines: Xe. The profiles for the variable HS model are not shown, since for $\omega = 0.66$ and 0.85 the results are close to that of the HS model and He, respectively.

where $n_w = -2\sqrt{2\pi/T_0}\int_{v_2<0} f v_2 dv$. At $x_2 = 0$, we have $f(v_1, v_2, v_3) = f(v_1, -v_2, -v_3)$ for $v_2 < 0$ due to symmetry.

The profiles of macroscopic quantities and reduced VDFs when $\delta = 0.1$ are shown in Figs. 4 and 5, respectively, where we see that the relative difference in gas velocity is close to that in the linearized Couette flow, and the use of the variable HS model only slightly improves the accuracy. The reduced VDF also has a relatively large difference between the noble gas and the HS gas at $v_2 \sim 0$. The shear stresses in the various gases are, however, very close to each other in nonlinear Couette flow. This is because the gas temperature is around T_0 so the rarefaction parameters are nearly the same. Therefore, if only the shear stress is of interest, the HS model can be used.

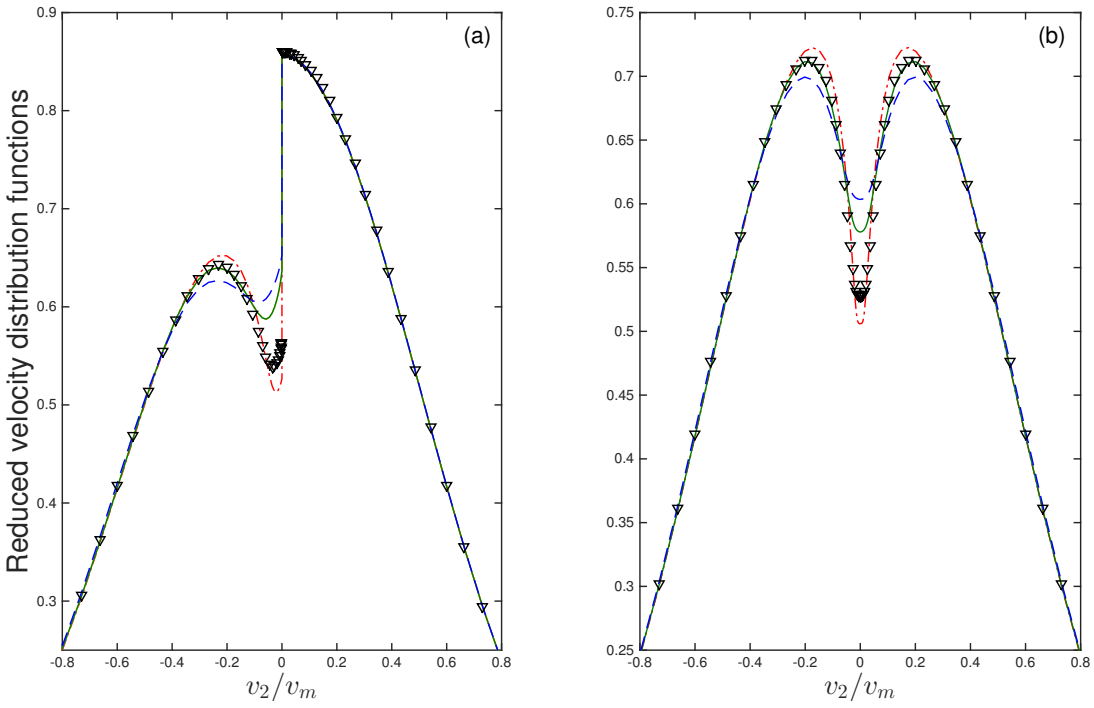

FIG. 5. Reduced VDFs $\int f dv_1 dv_3$ in the nonlinear Couette flow at $\delta = 0.1$. (a) $x_2 = -0.5$, (b) $x_2 = 0$. Dash-dotted lines: HS gas; Solid lines: He; Dashed lines: Xe. Triangles: variable HS model with viscosity index $\omega = 0.85$. The reduced VDF for the variable HS model with $\omega = 0.66$ is not shown, since it nearly overlaps that of the HS model.

VI. CONCLUSIONS

We have presented a general fast spectral method to solve the Boltzmann equation with arbitrary intermolecular potentials. Specifically, through comparison with results from the variational and discrete velocity methods, we have demonstrated the accuracy of the FSM for the realistic (6-12) LJ potential. As an application, the FSM has been applied to planar Fourier and Couette flows. Our results indicate that, for the same value of rarefaction parameter, the differences in the heat flux in Fourier flow, and the differences in the shear stress in Couette flow, are small between various noble gases. However, differences in other macroscopic quantities, and in the reduced velocity distribution functions, are large when the rarefaction parameter $\delta \lesssim 1$. For instance, when $\delta = 0.1$, the relative difference in the HS gas and Xe densities in Fourier flow is about 40%, while the relative difference in velocities in Couette flow is about 22%. In the nonlinear Couette flow considered in this

paper, the relative difference in the reduced velocity distribution functions of the HS gas and Xe can reach 20% at some velocity grid points. These differences increase when the rarefaction parameter decreases. We have also found that the variable HS model provides a slightly better result than the HS model.

This is a new numerical method for the Boltzmann equation, and we have also indicated the region of the rarefaction parameter in which the Boltzmann equation with the hard-sphere potential can be applied. For linearized and nonlinear problems where temperature does not vary too much, and when only the heat flux in Fourier flow and the shear stress in Couette flow are required, the hard-sphere model can be safely adopted. Otherwise, the differential cross-section of a realistic intermolecular potential should be adopted when the molecular mean free path is comparable to, or smaller than, the characteristic flow length.

Although we have only considered one-dimensional flows here, the computational time required for the Boltzmann collision operator remains unchanged for two- and three-dimensional flows, as the molecular velocity space is always three-dimensional. Our proposed numerical method can also be applied to mixtures of monatomic gases using *ab initio* potentials[13].

ACKNOWLEDGEMENTS

This work is financially supported by the UK's Engineering and Physical Sciences Research Council (EPSRC) under grants EP/I036117/1, EP/I011927/1, and EP/K038621/1.

REFERENCES

[1]S. Chapman, T. G. Cowling, The Mathematical Theory of Non-uniform Gases, Cambridge University, Cambridge, 1970.

[2]G. A. Bird, Molecular Gas Dynamics and the Direct Simulation of Gas Flows, Clarendon Press, Oxford, 1994.

[3]K. Koura, H. Matsumoto, Variable soft sphere molecular model for inverse-power-law or Lennard-Jones potential, Phys. Fluids A **3** (1991) 2459.

[4]H. Hassan, D. Hash, A generalized hard-sphere model for Monte Carlo simulation, Phys. Fluids A **5** (1993) 738.

[5]J. Fan, A generalized soft-sphere model for Monte Carlo simulation, Phys. Fluids **14** (2002) 4399.

[6]M. N. Macrossan, μ-DSMC: A general viscosity method for rarefied flow, J. Comput. Phys. **185** (2003) 612627.

[7]L. Wu, C. White, T. J. Scanlon, J. M. Reese, Y. Zhang, Deterministic numerical solutions of the Boltzmann equation using the fast spectral method, J. Comput. Phys. **250** (2013) 2752.

[8]L. Wu, J. M. Reese, Y. Zhang, Solving the Boltzmann equation deterministically by the fast spectral method: application to gas microflows, J. Fluid Mech. **746** (2014) 53-84.

[9]S. K. Loyalka, Slip and jump coefficients for rarefied gas flows: variational results for Lennard-Jones and $n(r)$-6 potentials, Physica A **163** (1990) 813-821.

[10]F. Sharipov, G. Bertoldo, Poiseuille flow and thermal creep based on the Boltzmann equation with the Lennard-Jones potential over a wide range of the Knudsen number, Phys. Fluids, **21** (2009) 067101.

[11]H. Matsumoto, K. Koura, Comparison of velocity distribution functions in an argon shock wave between experiments and Monte Carlo calculations for Lennard-Jones potential, Phys. Fluids A **3** (1991) 3038.

[12]F. Sharipov, J. L. Strapasson, Direct simulation Monte Carlo method for an arbitrary intermolecular potential, Phys. Fluids **24** (2012) 011703.

[13]F. Sharipov, J. L. Strapasson, *Ab initio* simulation of transport phenomena in rarefied gases, Phys. Rev. E **86** (2012) 031130.

[14]F. Sharipov, J. L. Strapasson, Benchmark problems for mixtures of rarefied gases. I. Couette flow, Phys. Fluids, **25** (2013) 027101.

[15]A. Venkattraman, A. A. Alexeenko, Binary scattering model for Lennard-Jones potential: Transport coefficients and collision integrals for non-equilibrium gas flow simulations, Phys. Fluids **24** (2012) 027101.

[16]A. B. Weaver, A. Venkattraman, A. A. Alexeenko, Effect of intermolecular potential on compressible Couette flow in slip and transitional regimes, Phys. Fluids **26** (2014) 107102.

[17]F. Sharipov, G. Bertoldo, Numerical solution of the linearized Boltzmann equation for an arbitrary intermolecular potential, J. Comput. Phys. **228** (2009) 3345-3357.

[18]O. I. Dodulad, Y. Y. Kloss, D. O. Savichkin, F. G. Tcheremissine, Knudsen pumps modeling with Lennard-Jones and ab initio intermolecular potentials, Vacuum **109** (2014)

360-367.

[19]C. Mouhot, L. Pareschi, Fast algorithms for computing the Boltzmann collision operator, Math. Comput. **75** (2006) 1833-1852.

[20]L. Wu, J. M. Reese, Y. Zhang, Oscillatory rarefied gas flow inside rectangular cavities, J. Fluid Mech. **748** (2014) 350-367.

[21]S. Takata, H. Funagane, Poiseuille and thermal transpiration flows of a highly rarefied gas: over-concentration in the velocity distribution function, J. Fluid Mech. **669** (2011) 242259.

[22]H. Grad, Asymptotic theory of the Boltzmann equation. Part II. In Rarefied Gas Dynamics (ed. J. A. Laurmann), I (1963) 26-59.

[23]C. Cercignani, On Boltzmann equation with cutoff potentials, Phys. Fluids **10** (1967) 2097-2104.

[24]J. H. Ferziger, H. G. Kaper, Mathematical Theory of Transport Processes in Gases, North-Holland Publishing Company, Amsterdam, 1972.

[25]A. B. Weaver, A. A. Alexeenko, Revised variable soft sphere and Lennard-Jones model parameters for eight common gases up to 2200 K, J. Phys. Chem. Ref. Data **44** (2015) 023103.